

Identification of a turnover in the initial mass function of a young stellar cluster down to $0.5 M_J$

Matthew De Furio^{1,2*}, Michael R. Meyer³, Thomas Greene⁴, Klaus Hodapp⁵, Doug Johnstone^{6,7}, Jarron Leisenring⁸, Marcia Rieke⁸, Massimo Robberto^{9,10}, Thomas Roellig⁴, Gabriele Cugno¹¹, Eleonora Fiorellino^{12,13}, Carlo Manara¹⁴, Roberta Raileanu¹⁵, Sierk van Terwisga¹⁶

¹ Department of Astronomy, The University of Texas at Austin, Austin, TX 78712, USA

² NSF Astronomy and Astrophysics Postdoctoral Fellow

³ Department of Astronomy, University of Michigan, Ann Arbor, MI 48109, USA

⁴ NASA Ames Research Center, Space Science and Astrobiology Division, Moffett Field, CA 94035, USA

⁵ University of Hawaii, Hilo, HI, 96720, USA

⁶ NRC Herzberg Astronomy and Astrophysics, Victoria, BC, V9E 2E7, Canada

⁷ Department of Physics and Astronomy, University of Victoria, Victoria, BC, V8P 5C2, Canada

⁸ Steward Observatory, University of Arizona, Tucson, AZ 85721, USA

⁹ Space Telescope Science Institute, Baltimore, MD 21218, USA

¹⁰ Johns Hopkins University, Baltimore, MD 21218, USA

¹¹ Department of Astrophysics, University of Zurich, Winterthurerstr. 90 CH-8057 Zurich, Switzerland

¹² Instituto de Astrofísica de Canarias, IAC, Vía Láctea s/n, 38205 La Laguna (S.C.Tenerife), Spain

¹³ Departamento de Astrofísica, Universidad de La Laguna, 38206 La Laguna (S.C.Tenerife), Spain

¹⁴ European Southern Observatory, Karl-Schwarzschild-Strasse 2, 85748 Garching bei Munchen, Germany

¹⁵ Department of Computer Science, University College London, London, UK

¹⁶ Space Research Institute, Austrian Academy of Sciences, Schmiedlstr. 6, 8042 Graz, Austria

* Corresponding author: defurio@utexas.edu

Abstract:

We present results exploring the initial mass function in a young (< 1 Myr) embedded star-forming region, NGC 2024, down to sub-Jupiter masses using the Near Infrared Camera (NIRCam) on the James Webb Space Telescope (JWST). Predominant star formation theory predicts a mass limit for the formation of objects produced through the fragmentation of molecular clouds, $2\text{-}10 M_J$. Previous studies identified an increasing mass function from the hydrogen-burning limit down to $\sim 10 M_J$, but were not sensitive to lower mass objects. In GTO-1190 (PI: M.R. Meyer), we obtained deep imaging of the central core of NGC 2024, covering $0.7 - 5 \mu\text{m}$ and sensitive down to $0.5 M_J$, and extracted photometry for 48 candidate members of the cluster. We find that a broken power-law model of the mass function best represents the data, increasing from $60 M_J$ to $12 M_J$ then followed by a decrease down to $0.5 M_J$. This is the first evidence for a decrease in the mass function below $10 M_J$ in a stellar population. Our program probes the lowest masses theoretically produced through star formation processes, finding no likely cluster members below about $3 M_J$, potentially the fundamental limit of the star and brown dwarf formation process.

Summary:

A successful theory of star formation should predict the number of objects as a function of their mass produced through star-forming events. Previous studies in star-forming regions and the solar neighborhood identify a mass function increasing from the hydrogen-burning limit down to about $10 M_J$ ^{20,21}. Theory predicts a limit to the fragmentation process³⁸, providing a natural

turnover in the mass function down to the opacity limit of turbulent fragmentation thought to be 2-10 M_J . Programs to date have not been sensitive enough to probe the hypothesized opacity limit of fragmentation¹⁶. Here we present the first identification of a turnover in the initial mass function below 12 M_J within NGC 2024, a young star-forming region. With JWST/NIRCam deep exposures across 0.7-5 μm , we identified several free floating objects down to $\sim 3 M_J$ with sensitivity to 0.5 M_J . We present evidence for a double power law model increasing from about 60 M_J to roughly 12 M_J , consistent with previous studies, followed by a decrease down to 0.5 M_J . Our results support the predictions of star and brown dwarf formation theory, identifying the theoretical turnover in the mass function and suggest the fundamental limit of turbulent fragmentation near 3 M_J .

Text:

Many surveys have attempted to characterize the mass function down to Jupiter mass scales in the Galactic field, the halo, star clusters²⁷, and in young, star-forming regions. Early studies in the Galactic field modeled the mass function as a broken power law ($dN \propto m^{-\alpha}$) and calculated a power law index over 0.01-0.08 M_\square as $\alpha = 0.3 \pm 0.7$ ²². More recent work characterized the mass function using stars and brown dwarfs within 20 pc and found $\alpha = 0.6 \pm 0.1$ for 0.01-0.05 M_\square ^{20,21}. Microlensing surveys are sensitive to free-floating super-Earths, and found that a mass function with a power law index of $\alpha = 0.8$ with a 3σ confidence interval of [0.2, 1.3] for masses 0.01-0.08 M_\square ²⁸. However, none of these programs were able to characterize the initial mass function (IMF), the product of the star and brown dwarf formation process, below 0.01 M_\square .

With the launch of the James Webb Space Telescope (JWST), multiple programs were designed to detect free-floating planetary mass objects in young star-forming regions with the ultimate goal of identifying the opacity limit for fragmentation, i.e. the end of the IMF. While not characterizing the mass function, a NIRCam/NIRSpec program in IC 348 identified evidence for a 3-4 M_J cluster member with no lower mass objects identified²⁴. Similarly, a NIRISS study in NGC 1333 identified free floating planetary mass objects with estimated masses of 5-15 M_J without any observed lower mass sources, despite sensitivity to such objects²³. A recent study in the ONC claims to detect planetary mass objects with masses down to 0.6 M_J ²⁵, in contrast to the results we present below and that in IC 348²⁴ and NGC 1333²³. Yet, contamination from extragalactic sources may bias their results.

In order to characterize the IMF, we obtained JWST Near Infrared Camera (NIRCam) deep exposures of a single field (roughly 9.68 square arcminutes) in the core of NGC 2024, a young (< 1 Myr), compact star-forming region. This region is nearby (400 pc)³¹, contains massive stars, and is highly extinguished with > 20 magnitudes of visual extinction to many known sources³¹, serving as a screen for many potential background contaminants while requiring deep exposures to detect free floating objects down to sub-Jupiter masses. We observed this region with eight separate medium and wide filters: F070W, F115W, F140M, F182M, F356W, F360M, F430M, and F444W (GTO-1190, PI: M.R. Meyer). These filters were chosen to cover a broad range of wavelengths specific to brown dwarf and free floating planetary mass object spectral energy distributions. We identified 100 point sources using an automated point source detection routine (see Methods) and obtained aperture photometry on all of our detections. We define flux limits across the entire field of view, resulting in some degree of sensitivity from apparent magnitude of

13.5 - 23.6 in the F430M filter and F182M - F430M color from 0 - 11.2 mag, see Fig. 1. Our flux limits correspond to a 0.5 M_J object with $A_V = 0$ mag, a 1 M_J object with $A_V \sim 30$ mag, and a 2 M_J object with $A_V \sim 50$ mag. Accounting for saturation, we remove sources with F182M ≤ 16 mag or F430M ≤ 13.5 mag corresponding to stars and high mass brown dwarfs which are not included in our analysis.

NGC 2024 has a prominent ridge of ambient molecular material producing $A_V > 100$ mag through large portions of the region. Due to the proximity of the cluster and the field of view of the data, we anticipate zero foreground objects that would resemble brown dwarf members. However, the extinction is spatially variable, allowing for both background Galactic field stars and extragalactic sources to appear in our data as faint point sources. We evaluated the likelihood of each point source being a contaminant by simulating a Galactic field population using the TRILEGAL tool¹⁷ and incorporating the Jaguar Mock Catalog³⁹ (consistent with observations of JADES program) to simulate the extragalactic population. For each point source, we estimate a maximum extinction if the source were truly background using the Herschel Gould Belt Survey (HGBS) molecular hydrogen column density maps^{5,29} and the relation: $N(\text{H}_2) = 0.94 \times 10^{21} \times A_V [\text{cm}^{-2} \text{mag}^{-1}]^{7,32}$. We then project the simulated Galactic and extragalactic populations into color-magnitude space in many combinations of our filter sets. Finally, for each point source we calculate the expected number of background contaminants given its color-magnitude and the estimated extinction at its location. For our sample of 100 point sources, we identified 48 likely cluster members and 52 likely background objects.

In order to fit a mass function to our data, we used a Bayesian framework to incorporate both the information from our likely cluster member detections and our sensitivity across the field of view, accounting for incompleteness, see Fig. 1. First, we define the mass function as a power law, similar to previous work in the Galactic field^{20,21}, $N = C \int m^{-\alpha} dm$, where α is the index of the power law and N is the total number of objects across our full mass range and all extinctions $A_V = 0-100$ mag. Our bounds are 0.0005 - 0.062 M_\odot , the extent of the ATMO2020 atmospheric models³⁰ for 1 Myr, with C as an integration coefficient. We are sensitive to higher masses through larger extinction, but for this analysis we ignore higher masses where saturation is an issue. We analyze the F430M and F182M-F430M color-magnitude diagram, which includes the largest number of objects in the sample for a given color-magnitude combination (26) and probes the lowest masses attainable with our survey, 0.5 M_J .

We utilize the Bayesian inference technique, PyMultiNest⁹ that performs the Nested Sampling Monte Carlo analysis¹⁴. For each fit to the data, PyMultiNest calculates the Bayesian evidence, a value we can use to compare different models. We define the likelihood function based on Poisson statistics and convert the sampled mass function and extinction into color-magnitude space and evaluate the likelihood that we would detect these sources given our survey sensitivity. We also produce a joint probability distribution given each sampled mass function and the known sensitivity of our survey, and calculate the probability of each model given the color-magnitude of our true detections (shown in Fig. 1), following prescriptions provided for other Bayesian analyses^{12,15}.

For the single power-law case, we sample values of $N = [1, 100]$ and $\alpha = [-3, 3]$. From our sample of 26 detected sources in the F182M and F430M filters, we derive 95% confidence

intervals of $N = 43 +17/-16$ and $\alpha = 0.34 +0.33/-0.37$, see Fig. 2. We also fit alternative mass function models (a single power law with a low-mass cutoff, a log-normal distribution, and a normal distribution) that return a difference in log-evidence < 2 relative to the best fit of the single power law, or a probability < 0.92 that these models are favored over the single power law model³⁴. Lastly, we fit a double power law model, defining the mass function as $N = C_1 \int m^{-\alpha_1} dm + C_2 \int m^{-\alpha_2} dm$, where N is as above, α_1 is the power-law index for the low-mass portion of the mass function integrated from $0.0005 M_\odot$ to the break-point mass (where the two power laws differentiate), and α_2 is the power law index for the high-mass portion of the mass function integrated from the break-point mass to $0.062 M_\odot$. For this model, we sample values of $N = [1, 100]$ and $\alpha_1 = [-3, 3]$, $\alpha_2 = [-3, 3]$, and the break-point mass $[M_\odot] = [0.001, 0.061]$. We derive 95% confidence intervals of $N = 41 +18/-17$, $\alpha_1 = -1.03 +1.07/-1.83$, $\alpha_2 = 0.34 +1.22/-1.63$, and the break-point mass = $0.0120 +0.0087/-0.0015 [M_\odot]$ over mass= $0.0005-0.062 M_\odot$ and $A_V=0-100$ mag, see Fig. 2. Importantly, the difference in the log-evidence between this double power law model and the single power law model is 8.2 which has a probability > 0.993 that the double power law model is favored over the single power law model³⁴. Among all the models we tested, the double power law model with a break-point mass is highly favored to best resemble the results of our survey.

As a check on our analysis, we compared the single and double power law models generating the artificial population with a sampled extinction distribution derived from the 26 detections in Fig. 1 instead of a uniform distribution from $A_V=0-100$ mag. We found no change in either Bayesian evidence after applying different extinction distributions for the single and double power law models, and found a slight increase in the power law index for the low mass portion of the mass function, consistent within the errors. We also compared the single and double power law models with uniform A_V distribution placing hard minimum sensitivity cutoffs in our survey field of view at 80, 90, and 95% instead of the chosen full range of sensitivity, see Fig. 1, and found a similar difference in the Bayesian evidence. The only change was the median of the low-mass power law index (α_1) that increased from -1.03 for the full sensitivity case to -0.89, -0.75, and -0.50 for the 80%, 90%, and 95% sensitivity cutoffs, respectively. This is due to the reduced ability to recover low-mass sources for higher sensitivity cutoffs. Since our Bayesian approach accounts for the incompleteness of our survey, we chose to allow the full range of sensitivities to place constraints on the mass function.

For our double power law model, the indices for the low and high mass end are within the respective 95% confidence intervals, due to the small number of detections in our sample. Additionally, the high-mass ($\sim 12-62 M_J$) power law index ($\alpha_2 = 0.34 +1.22/-1.63$) is comparable to the single power law index ($\alpha = 0.34 +0.33/-0.37$) over $0.0005-0.062 M_\square$. The low mass ($\sim 0.5-12 M_J$) power law index for our double power law model has a 95% confidence interval of $\alpha_1 = [-2.86, 0.04]$, overlapping the 95% confidence interval of the power law index for the single power law model. We do not have a strong constraint on these power law indices due to the sample size, however the Bayesian evidence strongly supports a model that rises from about $62 M_J$ to $12 M_J$ that then turns over and decreases down to $0.5 M_J$. This is the first evidence for a turnover in the mass function below $12 M_J$ in any stellar population to our knowledge.

With the results of our Bayesian analysis, we can compare to previous surveys in order to characterize the mass function below the theoretical limit of turbulent fragmentation, $\sim 2 M_J$ ^{8,38}.

Our single power law model is consistent with the previous results in the Galactic field: $\alpha = 0.3 \pm 0.7$ over $0.01-0.08 M_{\square}^{22}$, $\alpha = 0.6 \pm 0.1$ for $0.01-0.05 M_{\square}^{20,21}$, and $\alpha = 0.8$ with a 3σ confidence interval of $[0.2, 1.3]$ over masses $0.01-0.08 M_{\square}^{28}$. For our double power law model, we directly compare the posterior probability distributions for the low mass and high mass regions to these other surveys by randomly sampling their value of α given their error bars. For each random sample, we then integrate the posterior distribution of α_1 and α_2 from that value to infinity to arrive at the portion of the posterior that overlaps the single power law models of other studies. Compared to early results in the Galactic field²², we find a mean integrated probability of 0.09 and 0.69 relative to the low mass and high mass power law indices, respectively, i.e. no evidence for a difference. To more recent results in the field^{20,21}, we find a mean integrated probability of $2.0e-4$ and 0.61 for α_1 and α_2 , respectively. Relative to microlensing studies²⁸, we find a mean integrated probability of $1.6e-4$ and 0.69 for α_1 and α_2 , respectively. These results show strong evidence for a difference in the power law for the low mass portion of the mass function and previous results in the field down to $0.01 M_{\square}$, supporting our key finding, a turnover in the mass function below $\sim 12 M_J$.

Other surveys in young, star-forming regions also probe the low mass end of the mass function. Recent reviews report that most studies in star-forming regions identify a power law index $\alpha \lesssim 0.5$ below the hydrogen burning limit and down to $\sim 0.03 M_{\square}$, although studies at the time were not able to place strong constraints on α ⁶. A study in Upper Sco²⁶ was sensitive down to $\sim 10 M_J$ and found results consistent with the Galactic field results²⁰. Other studies² performed a meta-study of seven star-forming regions and used the ratio of stars to brown dwarfs (all $> 0.03 M_{\square}$) to compare to models of the mass function. They found that their observations agree with IMF models and suggest a decrease in the mass function into the substellar regime¹⁰, although without the sensitivity to Jupiter mass objects. A recent study in the Orion Nebula Cluster (ONC) with the Hubble Space Telescope found $\alpha = 0.6 \pm 0.06$ down to $\sim 5 M_J$ ¹⁶, providing 68, 95, and 99% errors. The high mass end of our double power law model is consistent with these results with a mean integrated posterior probability of 0.62, but the low mass portion of our double power law model has a mean integrated probability of $3e-4$, just as with the field population. Again, this comparison supports our identification of a break in the mass function down to Jupiter masses.

Our observations cover the core of NGC 2024, potentially biasing results to the environmental dependencies of the star formation and evolution process, previously shown in NGC 2024 for the stellar disk population³⁶. It may be difficult to produce low mass dense cores that will eventually become Jupiter mass objects within the high stellar density regions of clusters or near ionizing sources, potentially requiring quiescent portions of the cluster for formation. Previous results in NGC 1333 and the ONC suggest that brown dwarf formation is environmentally dependent within a cluster, where brown dwarfs form more often closer to other brown dwarfs as opposed to stellar cluster members^{3,18}. Also, if extinction is a function of mass of the objects, then our modeling of the mass function would be biased, however there is no evidence for a mass dependent extinction distribution in our data nor the literature. Additionally, unresolved binaries could cause the measured photometry and subsequent mass function modeling to overestimate the flux and mass of individual sources. Assuming a 15% companion frequency^{12,15}, four objects could be unresolved binaries. The low number of expected unresolved binaries leads us to conclude that the shape of the mass function is likely unchanged within the errors with a

potential decrease in the break-point mass, conserving the turnover in the mass function. In GO-5409 (PI: M. De Furio), we will obtain NIRSpec/MSA prism spectra of all likely sub-stellar cluster members to determine membership and better estimate masses, and also obtain NIRCам photometry near the edge of the region to explore any environmental dependence.

Our observations in NGC 2024 are sensitive to $2 M_J$ objects with $A_V \sim 50$ mag and $1 M_J$ objects with $A_V \sim 30$ mag albeit with no detections in our survey below $\sim 3 M_J$. These data suggest a potential limit of turbulent fragmentation near the theoretically derived value of $\sim 2 M_J^{8,38}$. With these data, we can best model the mass function as a double power law with a breakpoint mass and identify the first turnover in the IMF within a stellar population down to $0.5 M_J$. These results have implications on planet ejection. The planet mass function rises to smaller masses³³, while our data indicate a falling mass function. The decrease in objects from 10 to $0.5 M_J$ indicates that ejected planets are not dominant among the observed population. Our work will serve as a benchmark for future programs devoted to exploring different galactic star-formation scenarios such as violent bursts in galaxies in the cores of giant ellipticals early in their formation that can produce a bottom-heavy IMF³⁵. Similar populations may exist in the Galactic halo, potentially representative of early star-formation in the Milky Way, that will be explored with surveys using JWST, the Rubin Observatory, and the Roman Space Telescope^{1,19}.

Methods:

Data

In this paper, we use the stage 2 *cal* files and stage 3 *i2d* files to perform our analyses. The saturation limit of a single group using readout pattern SHALLOW2 is 16 mag in the F182M filter corresponding to a $0.017 M_\odot$ object with $A_V = 0$ or a $0.06 M_\odot$ object with $A_V = 20$ at 400 pc, the estimated distance to NGC 2024³¹, using the 1 Myr isochrone of ATMO2020³⁰. The saturation limit of a single group in the F430M filter is 13.5 mag corresponding to $0.0485 M_\odot$ with $A_V = 0$ for a 1 Myr source at 400 pc. Throughout the data, there are many saturated stars and high mass brown dwarfs that are excluded from our analyses. We ignore any sources with at least one saturated pixel in the first group.

Point Source Detection

Many automated routines exist in order to detect point sources within a given image. They present ways to identify point sources and extract their astrometry and photometry within Hubble Space Telescope (HST) data^{4,13}. There are also new applications of these methods to JWST data for the NIRCам and NIRISS instruments^{40,41}. These algorithms are designed to work well in crowded fields with many point sources, but were not specifically designed for data with a large amount of extended emission from nebulosity.

The nebulosity within NGC 2024 extends throughout the entirety of our images in a variable, asymmetric structure with many filaments and knots. When attempting to run common point source detection algorithms on these data, many thousands of non-existent “point sources” are

identified throughout the nebulosity of the cluster. Other false positive detections are made to the extended wings of bright sources.

In order to combat the issues identified with previous algorithms, we developed our own process to filter out semi-resolved structures within the cluster, image artifacts, and features of other bright point sources. We first took the Stage 2 data products from the MAST archive (*cal*) for each dither position and each filter and estimated a background model using the MMMBackground function from Photutils. We model the background with a 30x30 pixel box size and a 5x5 pixel filter size. For each *cal* file from each dither position and each filter, we create this model and subtract it from our data to make background subtracted images.

Simply defining some detectable flux above the background limit is not sufficient across the entire field of view because of the significantly variable background. Therefore, we created small sub-arrays of 32x32 pixels across the entire field of view and then identified 5σ detections within each sub-array where σ is the standard deviation within the sub-array. We used the DAOSTarFinder function of Photutils in order to identify these candidate point sources, and included the [empirically derived](#) full width at half maximum (FWHM) as the input to the 2D-Gaussian assumed for each filter. In order to avoid false negatives emanating from sources appearing on the edges of the sub-arrays, each successive sub-array was created 16 pixels away in one direction from the previous sub-array in order to make sure that all point sources would be detected in at least one of our sub-arrays. For a given filter, we iterate this sub-array detection approach for each dither position, one sub-array at a time. If we make a 5σ detection within the sub-array, to count this source as a point-source candidate, we then require the centroid of this detection defined by DAOSTarFinder to be with 0.5 pixels (15.5 milli-arcseconds [mas] in the SW channel, and 31.5 mas in the LW channel) of the same detection in eight of the ten dithered images within the same filter, allowing for some error due to detector effects, cosmic rays, or low signal-to-noise producing larger uncertainties on the positions. We require that any point source is > 10 pixels away from a saturated pixel which is intended to remove false positives resulting from the wings of bright sources that saturate the detector. These processes filter out many detector effects like hot pixels from our list of possible point sources. This process also removes many false detections from the extended nebular emission both because a 5σ detection above the local sub-array background is much higher in these nebulous regions, and because the centroid of a potential detection is not consistent throughout all the dither positions because it is moderately spatially resolved extended emission. However, this approach does not filter out all of the detections of the extended wings of a bright PSF as their centroids are conserved across all dither positions due to conserved extended structure of PSFs. We then require each detection to be made within two or more filters, an average centroid distance 10 mas (SW channel) and 20 mas (LW channel) from the same source in another filter, in order to be classified as a candidate point source. Occasionally, some detections made on the extended wings of a bright PSF are still conserved because of the similar PSF structure between overlapping filters like F356W and F360M or F430M and F444W. After this automated routine, we are left with 118 point-source candidates that likely include some false positives from the extended wings of bright sources seen in similar positions in two filters.

To finalize our list of candidate point sources, we then evaluated the FWHM of each source within each filter. For each source, we performed a cubic spline in the x and y directions

beginning from the peak pixel of each dither position of the stage 2 *cal* files. We then averaged the FWHM in both directions and over all dithers to get the final FWHM value within a filter. We accepted a source as a point source if we measured the FWHM $< 1.25x$ the empirically stated FWHM within two or more filters, accommodating potential detector effects like the brighter/fatter effect for bright yet unsaturated sources as well as measurement error on very faint detections. This resulted in a final sample of 100 candidate sources. The 18 5σ detections that were identified as having significantly larger FWHMs appear to be mostly extended wings of PSFs, knots of nebulosity within the cluster, and extended objects that are likely galaxies given their presence in mostly red filters. This automated approach ensures that our sample of point sources is not dependent on manual or “by-eye” rejection and that our sensitivity is defined consistently across the entire field of view.

Photometry

To obtain photometry for each of the 100 sources in our sample, we first used the PHOTMJSR value in the header of each stage 3 *i2d* file to convert the units of the data from MJy/sr to counts/s. Then, we subtracted the mean sky background using an annulus with inner and outer radii of 0.2" and 0.3" in the short-wave channel and 0.3" and 0.4" in the long-wave channel. Then, we used a circular aperture with radius equivalent to 0.1" for the short-wave channel and 0.2" for the long-wave channel to arrive at the total flux in the aperture and divided by the corresponding [encircled energy fraction](#) for the filter in question, running from 70-78%. Finally, we calculate the Vega magnitude for each source using the [Zeropoints](#) of each filter provided by STScI.

For every source that was detected in two or more filters, we ran an additional check throughout all filters to determine whether the source was detected. Occasionally, easily identifiable sources in the red filters were not detected in F115W or F140M even though they were very bright yet unsaturated. The severe undersampling in F115W and detector effects like charge migration and the brighter-fatter effect will significantly distort the core of the PSF even if it is not saturated. This caused our initial algorithm to skip over bright sources in the blue filters due to a significantly different FWHM than the empirically derived relation. Therefore, this extra step is necessary to make sure all possible photometry is obtained for all detected point sources.

In Extended Data Figure 2, we present color-magnitude diagrams for sources that had photometry in the F182M and F430M filters. We plot the calculated photometry compared to 1 Myr isochrones from the ATMO2020 chemical equilibrium models with extinction vectors derived for JWST filters³⁷. The saturation limits of each filter are shown, corresponding to sub-stellar objects even through many orders of magnitude in extinction. Importantly, there is a clear degeneracy between age, mass, and extinction that makes it difficult to identify candidate members purely based on their colors. Background field stars and brown dwarfs or extragalactic objects with high extinction can be confused with lower mass brown dwarf members with less extinction. Therefore, we need to filter out likely background objects in order to identify likely cluster members.

Background Source Contamination

NGC 2024 has a prominent ridge in the core producing $A_V > 100$ mag. However, the extinction is spatially variable, allowing for the potential for background stars and galaxies to shine through and appear as faint point sources. We used the Herschel Gould Belt Survey (HGBS) H_2 column density maps^{5,29} to estimate the visual extinction expected at each point within our field of view, although the pixel size of Herschel is 3.0" compared to the 0.063" pixel of the long-wave channel. Across the ~ 9.68 arcmin field of view, we record A_V values from 8-220 mag using the relation: $N(H_2) = 0.94 \times 10^{21} \times A_V [\text{cm}^{-2} \text{mag}^{-1}]^{7,32}$. In this region, there is significant ionization that can result in excess free-free emission. This free-free emission adds to the flux recorded by Herschel, leading to overestimates of extinction at the highest values. Therefore, extinctions as high as 220 mag may be non-physical, but the spatial dependence of extinction is clear.

Two possible background contaminants exist for our sample: Galactic field stars/brown dwarfs and extragalactic objects. We simulated a Galactic field population using the TRILEGAL tool¹⁷. We input the coordinates for NGC 2024 and output a photometry table for the JWST/NIRCam filters in question using the default TRILEGAL prescriptions. Additionally, we downloaded the Jaguar Mock Catalog that simulates the expected distribution of galaxies for many JWST instruments and filters³⁹. For each catalog, we produced a grid in color-magnitude space in equally spaced bins of < 0.1 mag, then determined the distribution of galaxies and field objects expected within the full range of color-magnitude space, and normalized the distribution, see Extended Data Fig. 1. If a source were background, it would be consistent with these distributions of Galactic and extragalactic sources after the estimated extinction was applied. For each source in question, we have an estimated extinction from the HGBS data as well as measured photometry with errors. We first produce a normalized Gaussian distribution of the source color-magnitude given the observed photometry and measured errors calculated from either the error arrays or assumed to be 3%, whichever is higher. An assumption of 3% errors is based on the continuous calibration errors that appear to change for many filters and detectors throughout the run of JWST. We then apply the expected extinction at that same position to the background source distributions. We then calculate the amount of overlap between the two distributions summing the following metric over all color-magnitude space: $\sqrt{P_1 * P_2}$. This value tells us the fraction of overlap our source has with the background object distribution. Then, we multiply by the number of sources in each catalog and the ratios of the field of view in each catalog relative to our observations to arrive at the total expected number of background objects within our field of view with the estimated extinction and the color-magnitude of our target. We performed this analysis for these combinations of color-magnitude: F115W-F182M v. F182M, F140M-F182M v. F182M, F115W-F430M v. F430M, F140M-F430M v. F430M, F182M-F430M v. F430M, and F360M-F430M v. F430M. For our sample of 100 objects, if the expected number of contaminants was < 0.01 in one of the combinations of color-magnitude, we classified it as a likely cluster member. We identified 48 objects that survived the rejection process as likely cluster members with 52 classified as background objects and the expectation of < 1 false positive result. All of our sources except for one were either very likely to be a background contaminant or very unlikely to be a background contaminant in multiple combinations of color-magnitude, highlighting the robustness of this approach.

Bayesian Analysis and the Mass Function Model

In order to fit a mass function to our data, we used a Bayesian framework to incorporate both the information from our likely cluster member detections and our sensitivity across the field of view, accounting for the incompleteness, see Fig.1. First, we define a functional form for the mass function, such as a power law, similar to previous work in the Galactic field^{20,21}, $N=C \int m^{-\alpha} dm$, where α is the index of the power law and N is the total number of objects across our full mass range and all extinctions $A_v = 0-100$ mag. Our bounds are $0.0005 - 0.062 M_{\odot}$, the extent of the ATMO2020 atmospheric models for 1 Myr, with C as an integration coefficient. We are sensitive to higher masses through larger extinction, but for the sake of this analysis we ignore higher masses where saturation is an issue and the models end. We also only perform this analysis for the F430M and F182M-F430M combination of color-magnitude, which includes the largest number of objects in the sample and probes the lowest masses attainable with our survey.

We utilize the Bayesian inference technique, PyMultiNest⁹ that performs the Nested Sampling Monte Carlo analysis¹⁴. For each fit to the data, PyMultiNest calculates the Bayesian evidence, a value we can use to compare to other model mass functions. We define the likelihood function with two components, the first of which is based on Poisson statistics and evaluates the model given our sensitivity. To calculate this, we generate a mass function from the sampled values of α and then sample that mass function to produce an artificial population of 10^3 sources with random visual extinction = 0 - 100 mag. We convert the mass of each object into color-magnitude space using the ATMO2020 models and apply the random extinction. Then, we evaluate the likelihood that each artificial source would be detected given the sensitivity of our survey and normalize the sampled number of expected detections (N) to the number of artificially generated sources ($n=10^3$): $k = \sum p_i * N / n$ from $i=1$ to $n=10^3$ where p_i is the probability a source would be detected given our sensitivity (colormap in Fig. 1). Then we calculate the Poisson likelihood from the true number of detections in our sample ($d = 26$ in F182M and F430M) and the evaluated value k : $L_p = k^d * e^{-k} / d!$.

The second component of the likelihood calculation evaluates the probability of our true detections given the model. Following past prescriptions^{12,15}, we define a joint probability given our sensitivity (see Fig. 1) multiplied by the mass function after it is mapped into color-magnitude space over $A_v = 0-100$ mag. Then, we evaluate the joint probability of each sampled mass function given the observed color-magnitude of our true detections, p_j . Finally, we combined these two calculations to arrive at the likelihood of each sampled mass function model: $L = L_p * \prod p_j$ over $j=1$ to d . With PyMultiNest, we maximize the likelihood to place constraints on these mass functions models.

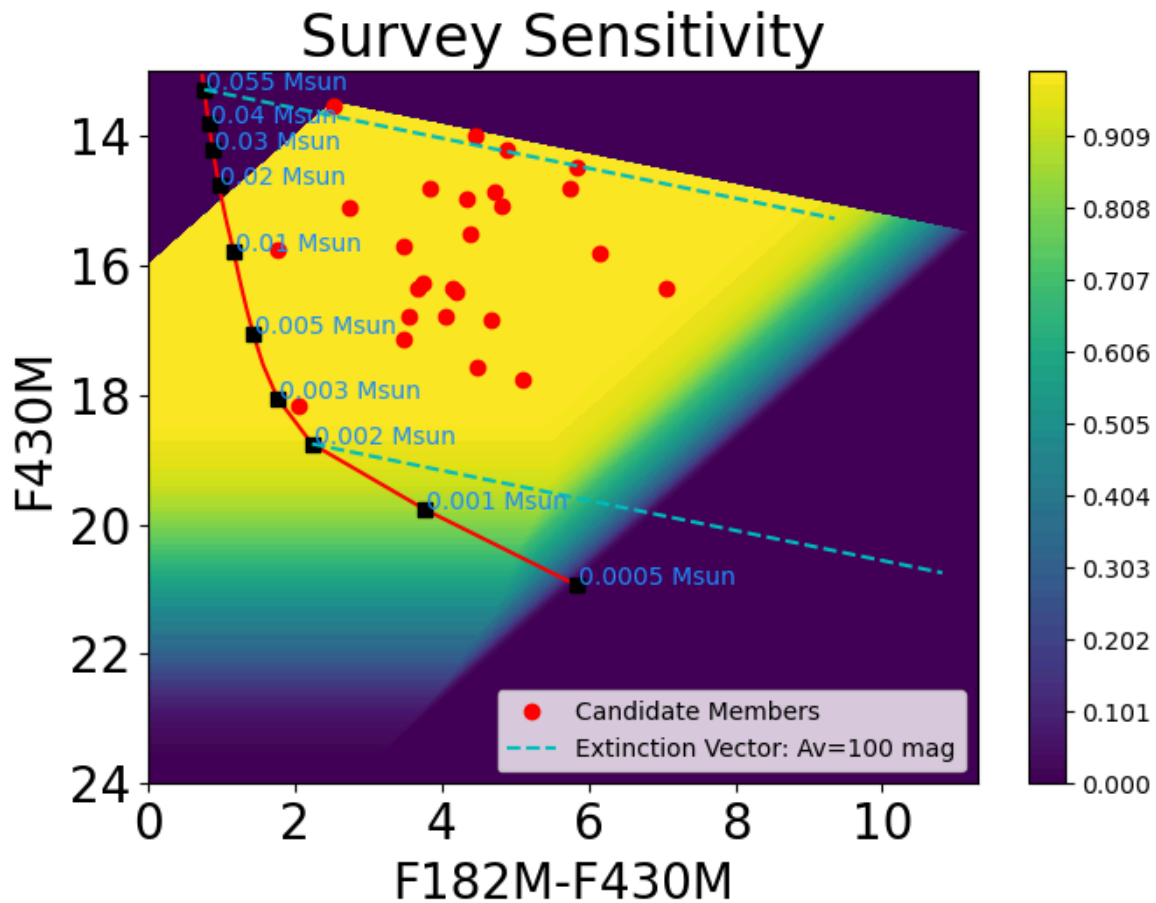


Figure 1. Sensitivity across the field of view of our NIRCcam data in the F182M and F430M filters. Color bar shows the fractional area from 1-100% that we are sensitive to a specific color-magnitude combination where a value of 1 corresponds to sensitivity over 100% of the field of view. The purple background has no sensitivity, either due to saturation or below our 5σ limit. Red circles are our likely cluster members. Cyan dashed lines are extinction vectors. The red line is the ATMO2020 chemical equilibrium 1 Myr isochrone where black circles with labeled masses are the color-magnitude corresponding to the given mass.

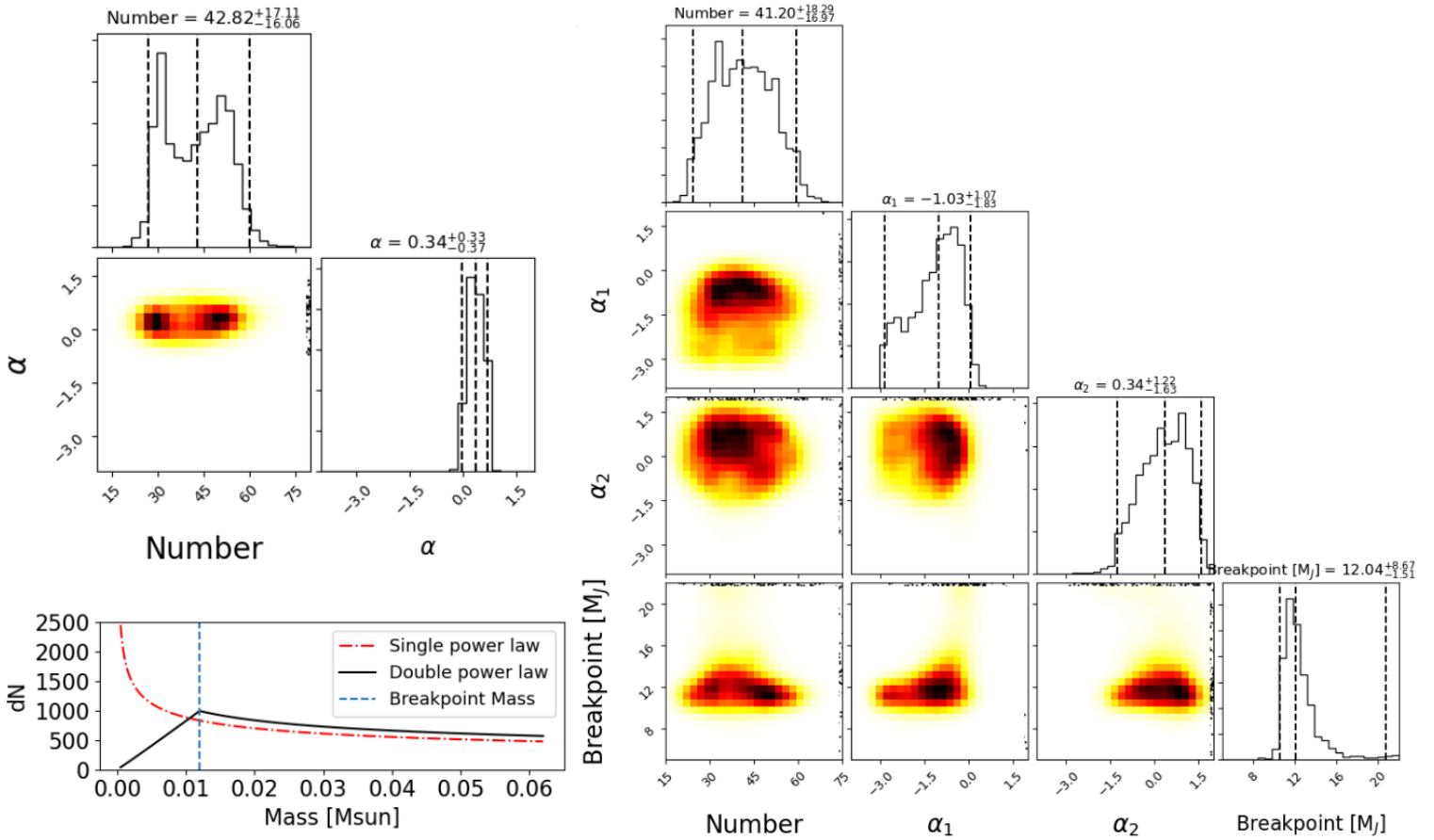
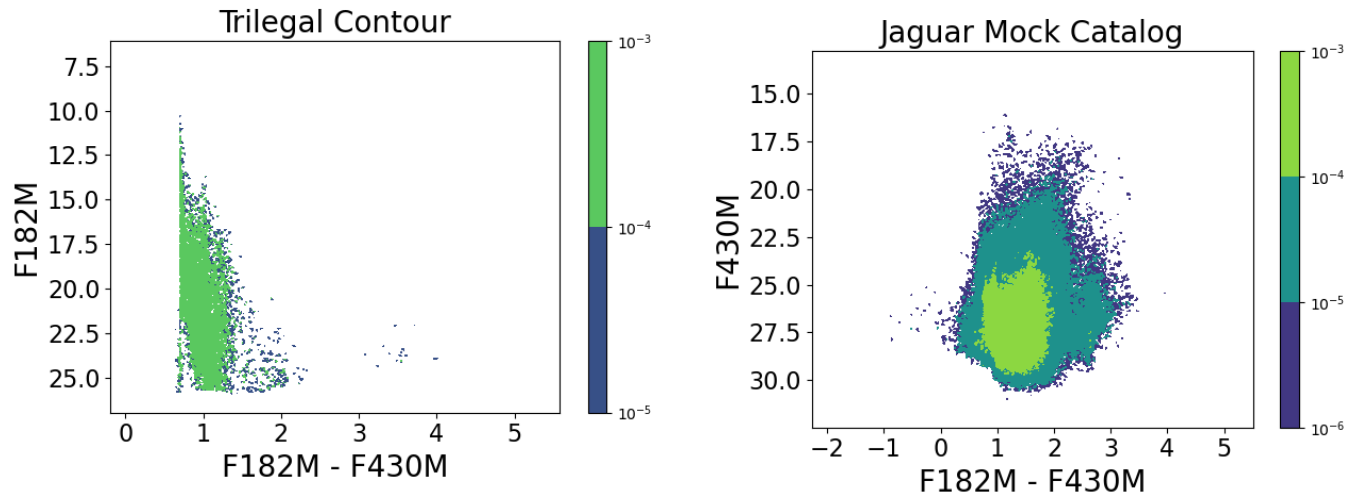
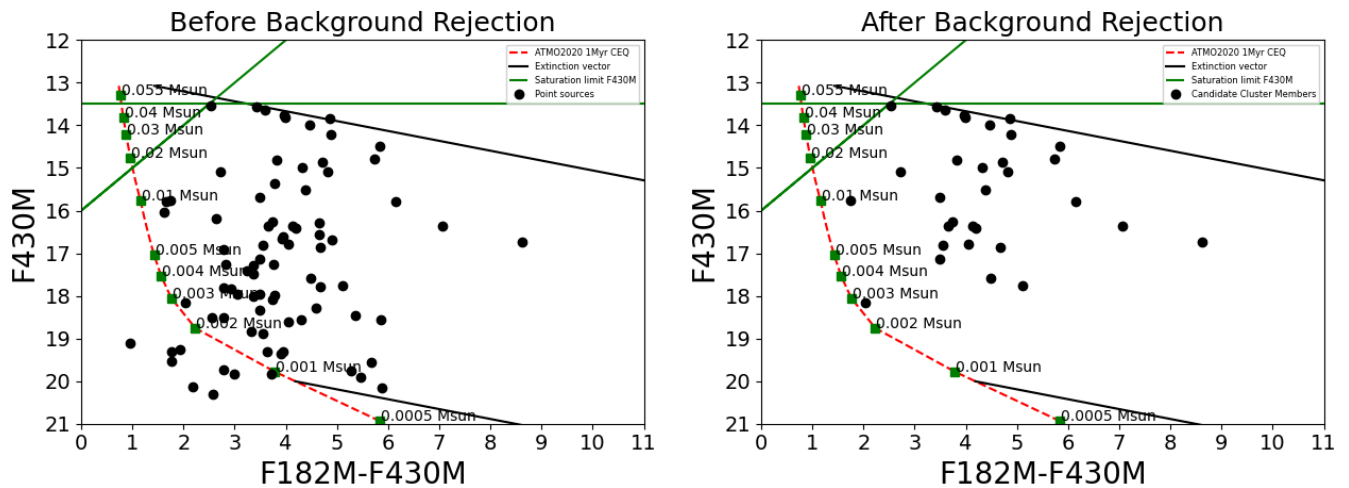


Figure 2. Corner plots for the single power law model (top left) and double power law model (right) over $0.0005 - 0.062 M_{\odot}$ and $A_v=0-100$ mag. *Number* is the number of expected sources over the mass and extinction range after accounting for incompleteness of our sensitivity, and α is the power law index for the single power law model. α_1 and α_2 are the power law indices for the low-mass and high-mass portions of the mass function, respectively. Breakpoint mass is the mass at which the two power laws diverge in units of M_J . Bottom left: median values for the single (red dot-dashed line) and double (black solid line) power law cases from our mass function fitting with the median value of the break-point mass (cyan dashed line). The best fit single power law model predicts many Jupiter mass objects while the best fit double power law model reflects a lack of objects down to $0.5 M_J$, as shown in our results.

Extended Data:



Extended Data Figure 1. F430M v. F182M-F430M diagram for the TRILEGAL (left) and JADES mock catalog (right) without any extinction applied. For all point source detections, we applied the corresponding extinction from the HGBS to both of these distributions and calculated the number of expected contaminants given the observed color-magnitude of our targets and normalized to the ratio of the areas of these catalogs to our field of view. All sources where the expected number of contaminants was < 0.01 were classified as candidate cluster members.



Extended Data Figure 2. F430M v. F182M-F430M before and after background rejection. Green lines are the saturation limits of the data for one group of the SHALLOW2 readout pattern. Black lines are extinction vectors. Red line is ATMO2020 chemical equilibrium 1 Myr isochrone within various masses labeled in the green squares. Left: black circles are point sources identified within the data. Right: black circles are the candidate cluster members within the data that have color-magnitude which would expect < 0.01 background contaminants in our field of view assuming the extinction from the HGBS.

References:

- [1] Aganze C., Burgasser A.J., Malkan M., Theissen C.A., Tejada Arevalo R.A., Hsu C.-C., Bardalez Gagliuffi D.C., et al., 2022, *ApJ*, 924, 114. doi:10.3847/1538-4357/ac35ea
- [2] Andersen, M., Meyer, M. R., Greissl, J., & Aversa, A. 2008, *ApJL*, 683, L183, doi: 10.1086/591473
- [3] Andersen M., Meyer M.R., Robberto M., Bergeron L.E., Reid N., 2011, *A&A*, 534, A10. doi:10.1051/0004-6361/201117062
- [4] Anderson, J., & King, I. R. 2006, Instrument Science Report ACS 2006-01, 34 pages
- [5] Andre, P., Men'shchikov, A., Bontemps, S., et al. 2010, *A&A*, 518, L102, doi:10.1051/0004-6361/201014666.
- [6] Bastian, N., Covey, K. R., & Meyer, M. R. 2010, *ARA&A*, 48, 339, doi: 10.1146/annurev-astro-082708-101642.
- [7] Bohlin, R. C., Savage, B. D., & Drake, J. F. 1978, *ApJ*, 224, 132, doi: 10.1086/156357
- [8] Boyd, D. F. A., & Whitworth, A. P. 2005, *A&A*, 430, 1059, doi: 10.1051/0004-6361:20041703
- [9] Buchner, J., Georgakakis, A., Nandra, K., et al. 2014, *A&A*, 564, A125, doi: 10.1051/0004-6361/201322971
- [10] Chabrier, G. 2003, *PASP*, 115, 763, doi: 10.1086/376392
- [11] Chabrier G., Lenoble R., 2023, *ApJL*, 944, L33. doi:10.3847/2041-8213/acadd3
- [12] De Furio, M., Liu, C., Meyer, M. R., et al. 2022, *ApJ*, 941, 161, doi: 10.3847/1538-4357/aca285
- [13] Dolphin, A. 2016, DOLPHOT: Stellar photometry, Astrophysics Source Code Library, record ascl:1608.013
- [14] Feroz, F., Hobson, M. P., & Bridges, M. 2009, *MNRAS*, 398, 1601, doi: 10.1111/j.1365-2966.2009.14548.x
- [15] Fontanive, C., Biller, B., Bonavita, M., & Allers, K. 2018, *MNRAS*, 479, 2702, doi: 10.1093/mnras/sty1682
- [16] Gennaro, M., & Robberto, M. 2020, *ApJ*, 896, 80, doi: 10.3847/1538-4357/ab911a
- [17] Girardi, L., Groenewegen, M. A. T., Hatziminaoglou, E., & da Costa, L. 2005, *A&A*, 436, 895, doi: 10.1051/0004-6361:20042352
- [18] Greissl, J., Meyer, M. R., Wilking, B. A., et al. 2007, *AJ*, 133, 1321, doi: 10.1086/510901
- [19] Hainline K.N., Helton J.M., Johnson B.D., Sun F., Topping M.W., Leisenring J.M., Baker W.M., et al., 2024, *ApJ*, 964, 66. doi:10.3847/1538-4357/ad20d1
- [20] Kirkpatrick, J. D., Gelino, C. R., Faherty, J. K., et al. 2021, *ApJS*, 253, 7, doi: 10.3847/1538-4365/abd107
- [21] Kirkpatrick, J. D., Marocco, F., Gelino, C. R., et al. 2024, *ApJS*, 271, 55, doi: 10.3847/1538-4365/ad24e2
- [22] Kroupa, P. 2001, *MNRAS*, 322, 231, doi: 10.1046/j.1365-8711.2001.04022.x
- [23] Langeveld, A., Scholz, A., Muzic, K., et al. 2024, *AJ*. accepted
- [24] Luhman, K. L., Alves de Oliveira, C., Baraffe, I., et al. 2024, *AJ*, 167, 19, doi: 10.3847/1538-3881/ad00b7
- [25] McCaughrean, M. J., & Pearson, S. G. 2023, arXiv e-prints, arXiv:2310.03552, doi: 10.48550/arXiv.2310.03552

- [26] Miret-Roig, N., Bouy, H., Raymond, S. N., et al. 2022, *Nature Astronomy*, 6, 89, doi: 10.1038/s41550-021-01513-x
- [27] Moraux E., Kroupa P., Bouvier J., 2004, *A&A*, 426, 75. doi:10.1051/0004-6361:20035669
- [28] Mroz, P., Udalski, A., Skowron, J., et al. 2017, *Nature*, 548, 183, doi: 10.1038/nature23276
- [29] Palmeirim, P., Andre, P., Kirk, J., et al. 2013, *A&A*, 550, A38, doi: 10.1051/0004-6361/201220500
- [30] Phillips, M. W., Tremblin, P., Baraffe, I., et al. 2020, *A&A*, 637, A38, doi: 10.1051/0004-6361/201937381
- [31] Robberto M., Gennaro M., Da Rio N., Strampelli G., Ubeda L., Sabbi E., Koeppe D., et al., 2024, *ApJ*, 960, 49. doi:10.3847/1538-4357/ad0785
- [32] Schneider, N., Osenkoff-Okada, V., Clarke, S., et al. 2022, *A&A*, 666, A165, doi: 10.1051/0004-6361/202039610
- [33] Suzuki D., Bennett D.P., Sumi T., Bond I.A., Rogers L.A., Abe F., Asakura Y., et al., 2016, *ApJ*, 833, 145. doi:10.3847/1538-4357/833/2/145
- [34] Trotta, R. 2008, *Contemporary Physics*, 49, 71, doi: 10.1080/00107510802066753
- [35] van Dokkum P.G., Conroy C., 2010, *Nature*, 468, 940. doi:10.1038/nature09578
- [36] van Terwisga S.E., van Dishoeck E.F., Mann R.K., Di Francesco J., van der Marel N., Meyer M., Andrews S.M., et al., 2020, *A&A*, 640, A27. doi:10.1051/0004-6361/201937403
- [37] Wang, S., & Chen, X. 2019, *ApJ*, 877, 116, doi: 10.3847/1538-4357/ab1c61
- [38] Whitworth, A. P., Priestley, F. D., Wunsch, R., & Palous, J. 2024, *MNRAS*, 529, 3712, doi: 10.1093/mnras/stae766
- [39] Williams, C. C., Curtis-Lake, E., Hainline, K. N., et al. 2018, *ApJS*, 236, 33, doi: 10.3847/1538-4365/aabcbb

Methods References

- [40] Libralato, M., Bellini, A., van der Marel, R. P., et al. 2023, *ApJ*, 950, 101, doi: 10.3847/1538-4357/acd04f
- [41] Weisz D.R., Dolphin A.E., Savino A., McQuinn K.B.W., Newman M.J.B., Williams B.F., Kallivayalil N., et al., 2024, *ApJS*, 271, 47. doi:10.3847/1538-4365/ad2600

Acknowledgements

We would like to acknowledge the early work and contributions that led to the planning of this program from Venu Suri and Karl Gordon. We are grateful for support from NASA through the JWST NIRCам project through contract number NAS5-02105 (M. Rieke, University of Arizona, PI). T. G. acknowledges support from the NASA Next Generation Space Telescope Flight Investigations program (now JWST) via WBS 411672.07.05.05.03.02. This work is based on observations made with the NASA/ESA/CSA James Webb Space Telescope. The data were obtained from the Mikulski Archive for Space Telescopes at the Space Telescope Science Institute, which is operated by the Association of Universities for Research in Astronomy, Inc., under NASA contract NAS 5-03127 for JWST. These observations are associated with program No. 1190. M.D.F. is supported by an NSF Astronomy and Astrophysics Postdoctoral Fellowship under award AST-2303911. D.J. is supported by NRC Canada and by an NSERC Discovery Grant. C.M. is funded by the European Union (ERC, WANDA, 101039452). Views and opinions expressed are

however those of the author(s) only and do not necessarily reflect those of the European Union or the European Research Council Executive Agency. Neither the European Union nor the granting authority can be held responsible for them. E.F. has been supported by project AYA2018-RTI-096188-B-I00 from the Spanish Agencia Estatal de Investigación and by Grant Agreement 101004719 of the EU project ORP. G.C. thanks the Swiss National Science Foundation for financial support under grant number P500PT_206785.

Author contributions

M.D.F. has led the data reduction/analysis and writing for this program and contributed to the observing planning. M.R.M., T.G., K.H., D.J., J.L., M.Ri., M.Ro., T.R., C.M., and R.R. contributed to the design and development of the science concept and observation plan as well as the interpretation of results and edits to the manuscript. G.C., E.F., and S.T. contributed to the interpretation of results and edits to the manuscript.

Competing interests

The authors declare no competing interests.

Materials & Correspondence

Correspondence and requests for materials should be addressed to M. De Furio.